Wall pressure unsteadiness and side loads in overexpanded rocket nozzles

Woutijn J. Baars[1] and Charles E. Tinney[2]
The University of Texas at Austin, Austin, TX, 78712, USA

Joseph H. Ruf[3], Andrew M. Brown[4] and David M. McDaniels[5]
NASA Marshall Space Flight Center, Huntsville, AL, 35812, USA

Surveys of both the static and dynamic wall pressure signatures on the interior surface of a sub-scale, cold-flow and thrust optimized parabolic nozzle are conducted during fixed nozzle pressure ratios corresponding to FSS and RSS states. The motive is to develop a better understanding for the sources of off-axis loads during the transient start-up of overexpanded rocket nozzles. During FSS state, pressure spectra reveal frequency content resembling SWTBLI. Presumably, when the internal flow is in RSS state, separation bubbles are trapped by shocks and expansion waves; interactions between the separated flow regions and the waves produce asymmetric pressure distributions. An analysis of the azimuthal modes reveals how the breathing mode encompasses most of the resolved energy and that the side load inducing mode is coherent with the response moment measured by strain gauges mounted upstream of the nozzle on a flexible tube. Finally, the unsteady pressure is locally more energetic during RSS, albeit direct measurements of the response moments indicate higher side load activity when in FSS state. It is postulated that these discrepancies are attributed to cancellation effects between annular separation bubbles.

---

[1] PhD Candidate, AIAA Student Member.
[2] Assistant Professor, AIAA Senior Member. http://www.ae.utexas.edu/facultysites/tinney/
[3] Aerospace Engineer, ER42/Fluid Dynamics Branch, AIAA Member.
[4] Lead Aerospace Engineer, ER41/Propulsion Structural & Dynamics Analysis Branch, AIAA Senior Member.
[5] Aerospace Engineer, ER42/Fluid Dynamics Branch.

Nomenclature

f = frequency, Hz

G = one-sided power/cross spectral density function, Pa^2/Hz (pressure) or N^2m^2/Hz (moment)

i = index of azimuthal pressure station

j = index of axial pressure station

L = number of azimuthal pressure stations

M = moment, N/m^2

Ma = Mach number

m = Fourier mode number

N = number of axial pressure stations

p = pressure, Pa

r = radius, mm

t = time, s

x = axial coordinate, along nozzle axis, mm

y = horizontal coordinate, normal to x, mm

z = vertical coordinate, normal to x, mm

α = fraction of resolved energy per Fourier mode

γ^2 = linear coherence function

Λ = total resolved energy, Pa^2

λ = resolved energy from one mode, Pa^2

θ = azimuth angle, rad or °

σ^2 = variance, Pa^2

Subscripts

0 = plenum, upstream of nozzle throat

a = ambient

atm = atmospheric

H = horizontal

M = location for computing moments

r = reattachment

s = separation

V = vertical

w = wall

Superscripts

$*$ = throat, $x = 0$

1 = 1^{st} separation bubble

2 = 2^{nd} separation bubble

P = based on pressure

S = based on strain

I. Introduction

During the transient start-up and shut-down of rocket nozzles used on liquid propellant fueled engines, off-axis forces are triggered by unsteady internal flow separation, and are occasionally enhanced by unsteady flow reattachment. The asymmetry of the internal flow structures results in a net lateral force, or side load. These side loads are severe enough that the operation of the engine and launch vehicle are endangered. For example, in the J-2S prototype engine, the successor of the J-2 Saturn V engine, a major failure was experienced when the engine was torn violently from its gimbal structure. Likewise, fatigue cracks and rupturing of the nozzle fuel coolant feed line surrounding the nozzle outer wall [1] have been identified on the Space Shuttle Main Engine (SSME) as a result of extreme side loads. Issues concerning excessive side loads have also been reported in Europe on the Vulcain engines [2] and in Japan on the LE-7A engine [3]. And so, an accurate assessment of these dynamic loads and a practical means by which they can be reduced is an important prerequisite for designing efficient, reusable and robust launch vehicles.

Depending on the nozzle contour and the nozzle pressure ratio (NPR), the overall features concerning the nature and location of the separated flow and shock structure comprise a lifecycle of different states. Foremost, many of the launch vehicles in operation today are designed with Thrust-Optimized Parabolic (TOP) contours. The shape of the throat region consists of a circular arc that transitions to the nozzle divergent wall that then extends to the nozzle exit plane. If there are discontinuities in the wall contour, a relatively weak internal shock forms slightly aft of the inflection point [4] which redirects the expanding flow to follow the non-ideal wall contour. Several optimization strategies can be pursued on the TOP contour to reduce the effect of unsteady and asymmetric flow separation. However, they involve manipulation of the diverging wall contour, which can adversely affect the thrust-to-weight ratio.

Various separated flow patterns can form inside nozzles while operating at highly overexpanded conditions and have been observed as far back as Arens & Spiegler (1963) [5], Nave & Coffey (1973) [6] and Schmucker (1973a&b) [7, 8]. During the transient start-up and shut-down of the TOP nozzle, the flow states can be classified into two categories: Free Shock Separation (FSS) and Restricted Shock Separation (RSS) as shown in figures 1 and 2. These illustrations are based on computational simulations performed at NASA Marshall Space Flight Center (MSFC) for this particular TOP nozzle.[29] In general, these schematics are similar to the models presented by Frey & Hagemann (2000) [4], Hagemann *et al.* (2002) [9] and Verma & Haidn (2009) [10]. However, deviations are attributed to the differences in the TOP nozzle contours, NPR values and test environments; the sub-scale nozzles used in experimental campaigns exhaust in a diffuser and ejector pipe that have different designs. In particular, Ruf *et al.* (2010a) [11] points out that the inlet of the ejector pipe can affect the location of flow separation and associated flow structures.

The first flow state, FSS, occurs at low NPRs and is illustrated in figure 1. The behavior of the FSS state is characterized by an incipient separation of the flow at x_s, which is triggered by an adverse pressure gradient between the region of isentropic expansion and the subsonic entrainment region. Compression waves, formed deep within the turbulent boundary layer, coalesce to form a

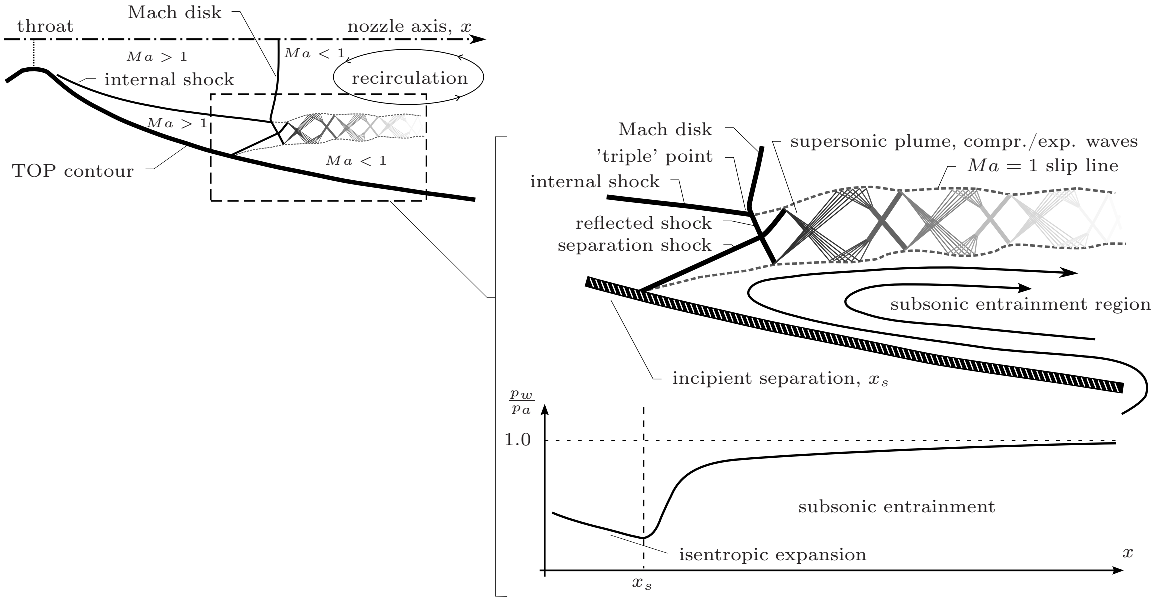

Fig. 1 Illustration of the internal shock structure during a Free Shock Separation (FSS) state in a TOP nozzle. A typical static wall pressure profile is schematically indicated in the right lower corner.

separation shock in the outer regions of the flow (outside of the boundary layer). This separation shock interacts with the reflected shock that originates at the so-called 'triple' point, where the Mach disk, internal shock and reflected shock coincide. A separated region encompassing a series of compression and expansion waves is located downstream of the shocks. At the lower NPRs, the separated flow does not reattach and the flow continues as a free supersonic jet and diffuses to subsonic speeds downstream due to mixing with the subsonic entrainment region and the low-speed recirculating core flow. The profile of the static wall pressure p_w is shown in the lower right hand corner of figure 1 in a normalized form by using the ambient back pressure p_a. The profile indicates a regular expansion up to the incipient separation point, thereafter, a rise to near ambient pressure is observed throughout the entire subsonic entrainment region.

When the NPR is increased in the TOP nozzle, the FSS state transitions to a RSS state which is indicated in figure 2. The incipient separation point is now located further aft with respect to the interaction point of the internal shock and Mach disk. The strong shock that originates from this interaction eventually results in outward radial momentum of the fluid that reattaches the supersonic plume to the wall. A bounded region of separated flow is now formed in between the separation shock and an expansion fan reflecting from the shear layer of the supersonic plume, further referred to as an annular separation bubble. Depending on the NPR, the annular supersonic jet might remain attached to the wall. However, it is believed that if the initial shocks (denoted by *separation shock* and *strong shock* in figure 2) are sufficiently strong, a shock (labeled *incident shock*) can appear which can separate the flow from the inner wall again through a shock wave turbulent boundary layer interaction phenomenon. The flow will presumably reattach further downstream, thereby creating a second separation bubble as indicated in figure 2. Where the static wall pressure is concerned, a pressure increase above ambient occurs in the separated regions. Once the flow reattaches, the flow expands and the pressure decreases up to the second separation point. For clarification, a rise in wall pressure does not necessarily indicate the presence of separated flow since the flow only separates if the incoming waves are strong enough. In the current experimental campaign a TOP nozzle was used where two separation bubbles were identified during RSS state by computational simulations. And so, in this article the first two rises in static wall pressure do provide an indication of the location of the first two separation bubbles. Finally, upon further increases in NPR, the RSS structure returns to a FSS state with an entrainment flow region that eventually vanishes once the nozzle flows full. It should be noted that nozzles with an ideal contour do not have the FSS → RSS transition; the flow resides in FSS state during the entire start-up due to the absence of the internal shock.

The most excessive side loads that have been observed during the entire transient cycle of the engine occur when the shock pattern transitions from FSS → RSS and RSS → FSS states. This has been reported in the experimental studies of Hagemann *et al.* (2002) [9] and Ruf *et al.* (2009) [1]. Östlund *et al.* (2004) [12] suggested that additional sources of side load disturbances are produced by fluctuating wall pressures in the separated regions of the nozzle, as well as aeroelastic fluid structure coupling; the latter was studied experimentally by Brown *et al.* [13]. Numerical models have also been developed to provide more insight into the origin of side loads during the full duty cycle of the engine. Chen *et al.* (1994) [14], for example, developed an unsteady compressible RANS simulation of a supersonic expanding flow to show the evolution of the separated region which included a contact surface, a slip stream behind the triple point, an initial shock front, shocklets and various sequential vortical and shock structures. In more recent years, transient, time-

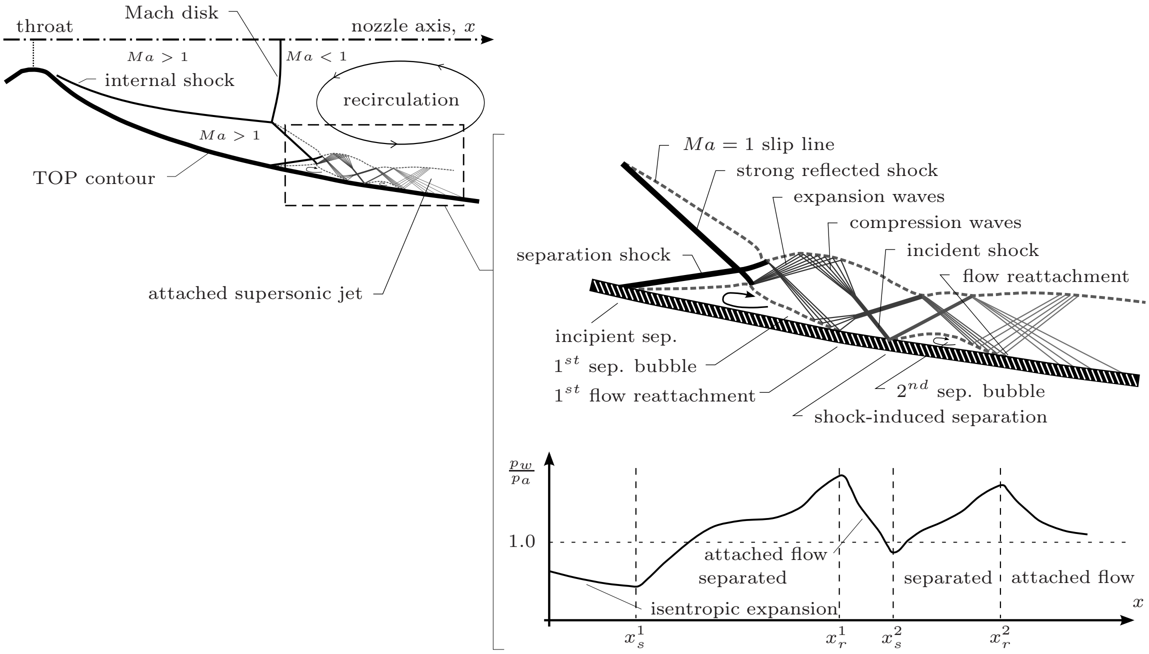

Fig. 2 Illustration of the internal shock structure during a Restricted Shock Separation (RSS) state in a TOP nozzle. A typical static wall pressure profile is schematically indicated in the right lower corner.

accurate numerical studies by Deck and Guillen (2002) [15], Schwane and Xia (2005) [16] and Wang (2009) [17] have provided additional details on the side load activity. However, while the overall findings from these computational efforts appear to coincide with the experimental observations, a clear understanding for the mechanisms governing the interaction zone remains unknown. With only a fraction of these simulations having incorporated the modern advancements in computational modeling, comprehensive quantitative datasets are still lacking to allow robust predictions of this behavior to be extended to more realistic conditions where experimental measurements appear impractical in the near future.

The focus of this article is to obtain better insight into the fluctuating surface pressure signatures and response moments that are invoked by unsteady pulsations of the shock structure and separated flow during both FSS and RSS states as they occur in a TOP nozzle. This is of considerable interest as increases in flow unsteadiness preceding each flow state transition (FSS → RSS and RSS → FSS) are believed to be plausible sources of transition [18, 19]. The unsteadiness of the FSS and RSS flow structures is illustrated in figure 3. The incipient separation front x_s^1 and reattachment line x_r^1 (for RSS only) are identified in this illustration and posses unsteady motions that vary in azimuth.

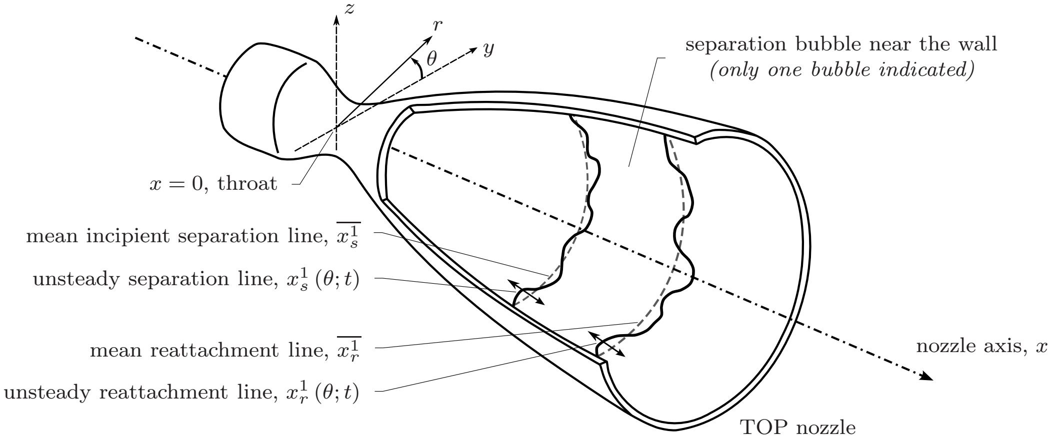

Fig. 3 Schematic of the unsteady motion of the incipient separation front and reattachment line during RSS flow state with one trapped separation bubble. Azimuthal variations cause asymmetric pressure distributions and ultimately result in off-axis side loads.

Thus, for the illustration encompassing one separation bubble during RSS state, $x_s^1 = x_s^1\,(\theta, t)$ and $x_r^1 = x_r^1\,(\theta, t)$. The resulting unsteady, azimuthal varying, wall pressure distribution results in off-axis forces as was described as one of the direct sources of side load activity by Östlund *et al.* (2004) [12]. The unsteady motions resemble many of the features observed in shock wave turbulent boundary layer interaction (SWTBLI) studies including the compression ramp studies by Erengil & Dolling (1991) [20] and the recent incident shock investigations of Humble *et al.* (2009) [21]. The most notable feature that has attracted much attention in SWTBLI studies is the significant discrepancy observed between the dominant low-frequency shock motion and the characteristic high-frequencies that correspond to the radiation of the turbulent boundary layer. Plausible explanations for this discrepancy continue to be debated, a review of which can be found in a recent discussion by Clemens & Narayanaswamy (2009) [22]. While the incipient separation during FSS conditions is induced by an adverse pressure gradient, the separation shock that forms presumably involves the same characteristic features as observed in SWTBLI studies. As for the RSS condition, the presence of the separation shock, the expansion waves reflecting from the downstream part of the separation bubble, and the incident shock in the partially attached supersonic plume inevitably complicate an identification of SWTBLI features, and so, a much more comprehensive analysis is expected under these conditions.

Analysis of the fluctuating wall pressures and response moments is furnished by detailed measurements of both the static and unsteady surface pressure signatures, as well as the response moments measured on a strain tube upstream of a sub-scale TOP nozzle. Fluctuations in the surface pressure and response moments are invoked by unsteady pulsations of the shock waves and separated flow. Several constant NPRs are selected which correspond to various states in the transient start-up cycle for which fluctuations are superposed a steady mean flow. Similar studies have been conducted by Nguyen *et al.* (2002,2003) [23, 24], Verma *et al.* (2006) [18] and Verma (2009) [19] and are used here to provide confidence for the measurements that are presented. It is believed that a detailed understanding of these unsteady pulsations is a prerequisite to developing robust and effective methods for reducing nozzle side loads.

II. Experimental Apparatus & Procedure

The experimental dataset used for the analyses was acquired in the Nozzle Test Facility at NASA MSFC. Cold-flow tests were performed using an axisymmetric TOP nozzle cantilevered on a strain tube, following the approach of Dumnov (1996) [25]. The entire assembly was mounted inside a vacuum chamber where the nozzle exhausts into an ejector pipe. Constant and transient NPRs were achieved by decreasing the vacuum chamber pressure while maintaining a constant plenum pressure and temperature, upstream of the nozzle throat, of $9.2atm$ ($135psia$) and $340K$, respectively. An illustration of the fully instrumented nozzle inside the vacuum chamber is shown in figure 4a alongside a schematic with the coordinate system of the nozzle and strain tube in figure 4b. The nozzle has a TOP contour and was designed to simulate the separated flow behavior observed during transient start-up of the SSME. The throat radius of the nozzle is $r^* = 19.05mm$ ($0.75in$) and has an exit-to-throat area ratio of 38. This exit-to-throat area ratio requires a NPR of $1,020$ to produce ideally expanded flow at a design exit Mach number of 5.58. However, full flowing conditions occur around a NPR of 200. The interested reader is referred to Ruf *et al.* (2010b) [26] for additional details describing the TOP nozzle and the Nozzle Test Facility at NASA MSFC.

Several axial and azimuthal arrays of pressure transducers were used to measure the static and dynamic wall pressure signatures on the interior surface of the nozzle. This consisted of two curvilinear arrays (nominally at $\theta = \pm\pi/2$) of 37 static pressure ports along the axial direction with constant axial spacings of $\Delta x/r^* = 0.45$. These static pressure ports spanned between $x/r* = 1.60$

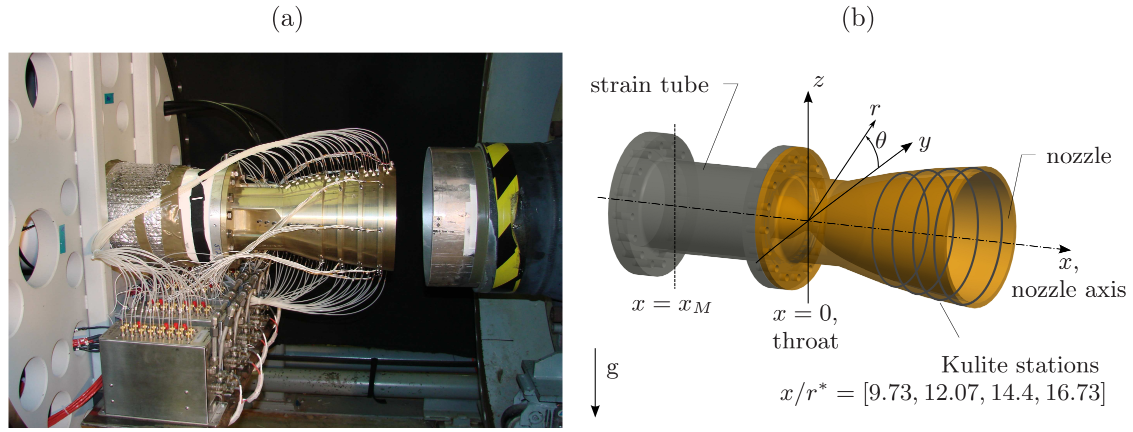

Fig. 4 (a) The fully instrumented TOP nozzle mounted in the Nozzle Test Facility at NASA MSFC, (b) Schematic overview of the nozzle/strain tube assembly with coordinate system.

and 17.80; the exit plane of the nozzle is located at $x/r^* = 18.40$. The static wall pressures were sampled at $500Hz$ and averaged over $0.25s$ intervals. As for the dynamic wall pressure signatures, a total of 32 high-frequency Kulite XT-140 transducers, mounted flush along the expanding surface of the nozzle, were sampled simultaneously at $20,480Hz$ for approximately 18 seconds at each of the four NPRs investigated. The arrangement of the transducers comprised four axial stations ($N = 4$) at $x/r^* = 9.73, 12.07, 14.40, 16.73$ (further referred to as $x_j,\ j = 1...N$), with each axial station comprising an azimuthal array of eight transducers ($L = 8$) with equal increments of $\Delta\theta = 45°$ ($\theta_i,\ i = 1...L$).

The focus of the current study will be on conditions corresponding to four constant NPR settings of 25, 30, 40 and 50 encompassing both FSS and RSS flow states. A typical time-series of the nozzle pressure ratio during the NPR 25 experiment is shown in figure 5a. The power spectral density (PSD) from a high-frequency pressure transducer located inside the vacuum chamber, outside of the nozzle, is shown in figure 5b. Several peaks are manifest and are attributed to various facility-induced disturbances including acoustic reflections from the ejector pipe and vacuum chamber.

The structural dynamic response of the nozzle/strain tube assembly, due to side loads induced by the unsteady internal flow, was measured with two pairs of full-bridge strain gauges fixed to the strain tube at $x_M = -280mm$ ($-11in$) and oriented to capture the y- and z-axis moments. The main purpose of this relatively flexible strain tube is to amplify the structural response to the asymmetric load. The strain tube is $305mm$ ($12in$) in length, which results in an eigenfrequency of

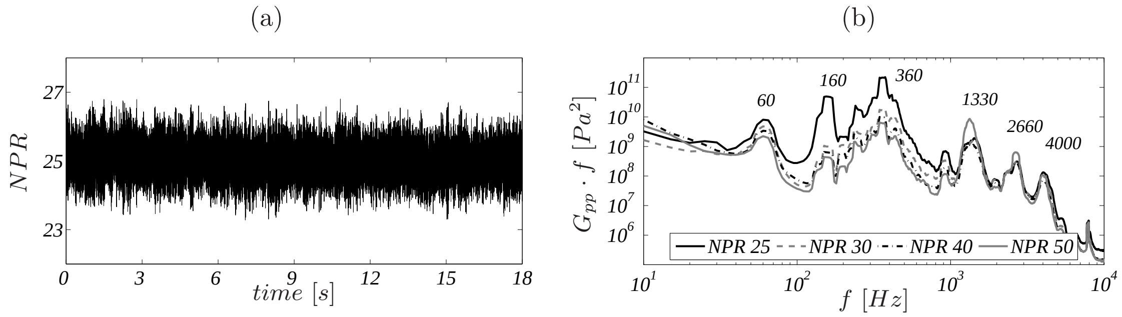

Fig. 5 (a) Time-series of the nozzle pressure ratio at NPR 25, (b) PSD of the vacuum chamber pressure (back pressure) during four fixed NPR conditions.

$187Hz$ for the combined nozzle/strain tube assembly. Resonance of the assembly was filtered from the raw strain gauge signals prior to data analysis, as described by Brown *et al.* (2009) [27]. To make valid comparisons between the various nominal NPR cases, all dynamic data (strain gauges and pressure) were scaled by the factor given in Eq. (1), where p_{atm} is the atmospheric pressure, here taken as $1atm$, and p_0 is the plenum pressure upstream of the throat and was $9.2atm$ for all test conditions. This scaling accounts for the decrease in absolute back pressure when increasing the NPR using the high-altitude vacuum chamber; in reality the back pressure remains constant during the transient cycle.

$$NPR_{scaling} = \frac{NPR \cdot p_{atm}}{p_0} \qquad (1)$$

III. Shock Separation States During Constant NPR Conditions

While the bulk of this analysis is focused on the dynamic pressure signatures, the static readings provide guidance for the appearance and location of the various flow features at each NPR. Therefore, static wall pressure distributions are presented in figure 6a-d. The profiles of the nominal NPRs (25, 30, 40 & 50) are shown, including a slightly lower and higher NPR to indicate the possible change in static wall pressures during a typical experiment. Alongside these static pressure profiles, the PSDs of the fluctuating wall pressure are shown in figure 6e-h and correspond to each nominal NPR condition. To aid in the discussion, several lines have been drawn in figure 6a-d corresponding to the shape of the nozzle contour and the four axial stations where the dynamic surface pressures were measured (labeled x_1 to x_4 in figure 6a). The ensemble averaged one-sided PSD functions were computed according to Eq. (2); the spectra were averaged in azimuth since the azimuthal variations were small and so the dynamic wall signatures are assumed to be statistically invariant in the mean sense. The spectra are presented in normalized form, $G(x_j; f) \cdot f/\sigma^2$, where σ^2 is the average variance of the eight azimuthal signals per axial location. Several distinct peaks in the spectra corresponding to facility-induced noise appear in these illustrations (figure 5b).

$$G\left(x_j; f\right) = \frac{1}{L} \sum_{i=1}^{L} \left\langle p\left(x_j, \theta_i; f\right) p^*\left(x_j, \theta_i; f\right)\right\rangle, \qquad \text{where} \quad p\left(x_j, \theta_i; f\right) = \mathcal{F}\left[p\left(x_j, \theta_i, t\right)\right]_t. \tag{2}$$

In figure 6a,e the NPR is 25 and the flow is in FSS state. The rapid rise in static wall pressure indicates the incipient separation location, shown here to occur around $x_s/r^* = 6$. All four axial locations comprising the azimuthal arrays of dynamic pressure are downstream of the incipient separation location and in the subsonic entrainment region. Two pronounced signatures are manifest in the PSDs in figure 6e. The first is dominated by low-frequency unsteadiness (between $10Hz$ and $250Hz$) and resides at the upstream location closest to the separation point and where the separation shock foot resides, while the second is associated with high-frequency broadband energy (between $2kHz$ and $10kHz$) and is predominant in the downstream regions near the nozzle lip. As expected, the PSDs found here resemble the fluctuating surface pressure signatures reported by Nguyen *et al.* (2003) [24] and Verma (2009) [19] (TOP nozzle studies), as well as the compression ramp and incident shock studies of Erengil & Dolling (1991) [20] and Humble *et al.* (2009) [21] (SWTBLI studies), respectively. The peaks in the PSDs in figure 6e are not the result of the FSS flow intermittently, or partially, transitioning to RSS (i.e. pRSS). By inspection of high-frequency pressure time signals in a dataset where the NPR was slowly increased it was indicated that pRSS flow began to appear at a NPR of about 27.5. Occasional spikes in the pressure time histories were observed at lower NPRs, but none with any regularity. Furthermore, the current measurements show the absence of a low-frequency hump at the last measurement station x_4, which is in agreement with the findings from the study by Verma (2009) [19] on a TOP nozzle, where a decrease in the low-frequency content with increasing distance from the intermittent region was observed. As for the high-frequency content observed at location x_4, the relatively broadband distribution of energy is indicative of the absence

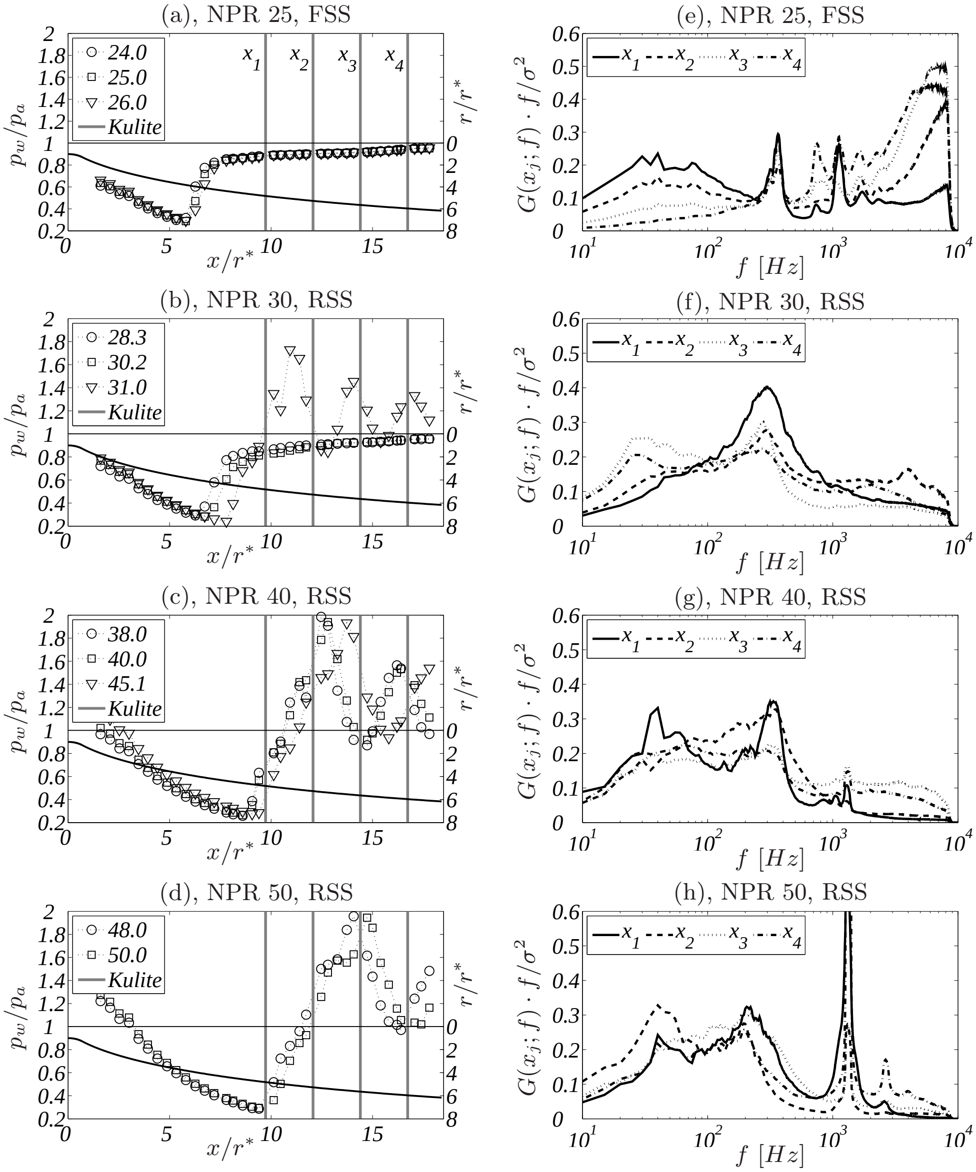

Fig. 6 (a)-(d) Normalized static wall pressure distributions for the nominal, and surrounding, constant NPR conditions. (e)-(h) PSDs of the fluctuating wall pressure at each of the four axial stations corresponding to the nominal NPR values.

of coherent structures in the entrained flow. This would suggest that the upstream unsteadiness is independent of the events entrained from the downstream regions of the nozzle, at least through a linear transfer (or excitation) of energy.

In figure 6b, the profiles of the static wall pressures are shown during the FSS state (NPR 28.3) for reference, and in the RSS state at two NPRs (30.2 and 31.0). For this specific nozzle, the FSS → RSS transition is found to occur when increasing NPR between 28 and 30. During the high-frequency measurements for the constant NPR 30 case, the flow was always in full RSS conditions. Upon transitioning from FSS → RSS, the incipient separation point shifts further aft by approximately $\Delta x/r^* = 1$ and is now located at $x_s^1/r^* = 8$. Two trapped separation bubbles are believed to have formed; the first bubble is centered at the first axial dynamic pressure measurement station, x_1. The static pressure in the reattachment region, at the downstream end of the first separation bubble, increases to almost 1.8 times the back pressure and occurs at $x_r^1/r^* = 11$. The second separation bubble spans axially from approximately $x_s^2/r^* = 12$ up to $x_r^2/r^* = 14$. The third axial region of rising wall pressure occurs due to shock impingement on the wall. It is believed that the last of these does not separate the flow, given the results provided from simulations performed at NASA MSFC. The low-frequency unsteadiness found in the PSDs of figure 6f are affiliated with individual pulsations of the annular separation bubbles and their interactions with the separation shock, expansion waves, and incident shock. However, unlike the FSS state, the low-frequency energy is more significant in the last two axial stations. This is understandable providing the fact that stations x_3 and x_4 are situated close to the reattachement region of the second separation bubble and subsequent region of shock impingement, respectively. A broadening of the low-frequency content of the spectra, peaking at about $300Hz$, is attributed to complex combinations of SWTBLI unsteadiness since annular separation bubbles are trapped between several shocks and expansion waves. The broadening of the spectra was also observed in the studies of Nguyen *et al.* (2002) [23] and Verma & Haidn (2009) [10].

Upon further increases in NPR to 40 and 50, the flow remains in RSS state. This time the incipient separation of the boundary layer occurs further downstream at respectively $x_s^1/r^* = 9$ and $x_s^1/r^* = 10$. For both cases, the static wall pressures in the first reattachment region rise to twice the ambient pressure. At NPR 50 the second separation bubble relaxes to ambient causing a 'semi' end-effect regime [6] to form along with a small region of unsteady reversed flow [19]. In the PSDs of figure 6g,h, low-frequency energy is again identified just downstream of the incipient separation line, x_1 for NPR 40 and x_2 for NPR 50. Since the first bubble is trapped between the separation shock and reflected expansion waves, the low-frequency energy can be attributed to a combined influence of wave motions.

IV. Pressure Induced Moments based on Integrated Wall Pressures

As a first approach to understanding the source of side loads during constant NPR conditions, a rational integration of the unsteady wall pressure signatures is performed. The contribution of each of the four axial segments, comprising eight high-frequency Kulite transducers per segment, are computed separately to isolate individual contributions to the side load unsteadiness. Figure 7 illustrates a wall surface element (i, j) corresponding to one transducer. The horizontal and vertical components of the moment at location $x = x_M$, caused by axial station j, is computed by integrating the dynamic wall pressure in azimuth according to

$$M_H^{P,j}(t) = -\sum_{i=1}^{L} p\left(x_j, \theta_i, t\right) sin\left(\theta_i\right) \left\{cos\left(\phi_j\right)\left(x_j - x_M\right) + sin\left(\phi_j\right) r_j\right\} A_j, \tag{3}$$

$$M_V^{P,j}(t) = \sum_{i=1}^{L} p\left(x_j, \theta_i, t\right) cos\left(\theta_i\right) \left\{cos\left(\phi_j\right)\left(x_j - x_M\right) + sin\left(\phi_j\right) r_j\right\} A_j, \qquad j = 1...4 \tag{4}$$

where r_j is the nozzle inner radius, ϕ_j is the local nozzle wall angle, and $A_j = 2\pi r_j\left(x_{j+1} - x_j\right)/8$ is the area of one element at location x_j.

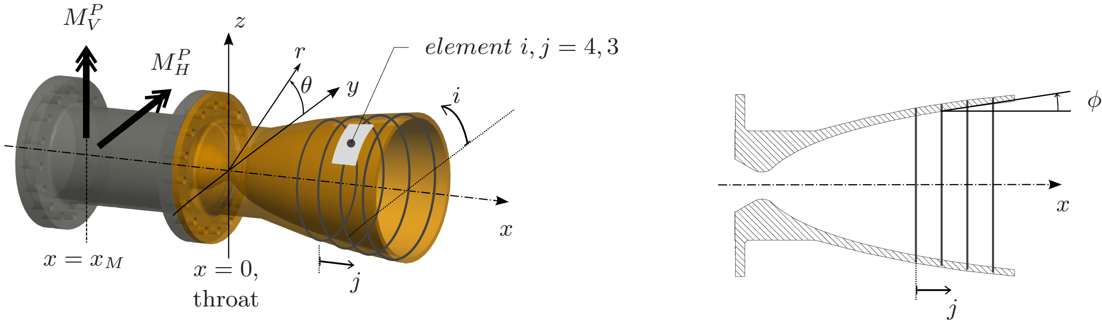

Fig. 7 Orientation of the experimental hardware for the prediction of the response moments (at $x = x_M$) based on integration of the dynamic wall pressures.

The individual moment contributions are presented in figure 8 as moment loci in time for each NPR run. The additional lines identify the mean of the moment magnitude (dashed white circle; and quantified by the value in the top right corner) and the region of 95% confidence (solid dark ellipse). The moment loci and 95% confidence ellipses are shown for a period of two seconds. The mean of the moment is computed from the entire dataset, roughly 18 seconds in length. In essence, differences between the two lines provide a visual indication of the preferred directionality of the moments that occur during 18 second time intervals.

In figure 8a (NPR 25, FSS state) only slight increases in moment amplitude occur when moving aft and is credited to the increase in moment arm length, surface area and absolute value of the pressure. The similarity in relative amplitudes are expected and are a consequence of the lack of any significant disturbances in this shock free, subsonic entrainment region. Thus, relative to the moment loci measured during RSS flow states (NPR 30 to 50), the azimuthal variation of the separation location $x_s(\theta, t)$, the formation of low-frequency pulsations in the subsonic entrainment region, or the high-frequency turbulent boundary layer signatures under the FSS flow state are either relatively axisymmetric throughout the entire separated region or too inconsequential to produce any significant side loads.

When the flow is in RSS state at a NPR of 30, the magnitude of the average moment increases considerably, as seen in figure 8b. In this instance, axial stations x_3 and x_4 produce most of the side load energy with the mean moment magnitude being roughly 4 to 5 times higher than in the FSS state. The low-frequency pulsating behavior captured by the last two measurement stations (located near the reattachment region after the second bubble and subsequent location of wave impingement) have greater asymmetry relative to the signatures registered at the first two axial stations. Thus, the principle driving force for side loads at NPR 30, based on a localized integration of the wall pressure, is produced by the asymmetries near the end of the nozzle. For reference, the first station is located in the center of the first separation bubble, and the second station is located in the attached flow region downstream of the second separation bubble. The unsteady phenomena at these locations are thus relatively axisymmetric.

At higher NPR settings (40 and 50), figures 8c and 8d, the sources of side load energy become more complicated, partly attributed to the coarseness of the dynamic pressure array in axial direction relative to the peaks and valleys in the static wall pressure profiles. At these two NPRs the smallest contributing source of side load activity is found near the incipient separation point. Consequently, the largest moment is found to reside at the reattachment region of the first trapped annular separation bubble, which resides around x_2 at NPR 40 and moves downstream to x_3 at NPR 50. The driving mechanism for this is believed to be the mean static pressure (twice the ambient pressure) combined with an asymmetric pulsation of this first reattachment line.

Based on these findings one might mistakenly assume that a spatial summation of the averaged magnitudes, that is,

$$M_H^P = \sum_{j=1}^{4} \frac{1}{T} \int_0^T M_H^{P,j}(t)\mathrm{d}t \qquad \& \qquad M_V^P = \sum_{j=1}^{4} \frac{1}{T} \int_0^T M_V^{P,j}(t)\mathrm{d}t \tag{5}$$

would pinpoint the RSS state at NPR 50 as being the dominant source of net side load activity ($715.2Nm$) with the other RSS states (NPR 30 and 40) contributing between roughly 73% and 80%, respectively. We will show later that this is indeed an overhasty assumption and that unsteady coupling between different axial stations produce uniquely different loads on the nozzle/strain tube assembly.

As for the directionality of the moment loci presented in figure 8, the phase angle θ in the (y, z)-plane for 0.25 seconds of data, at each NPR and all four axial stations, is shown in figure 9. The time-series are characterized by (1) low-frequency coherent like motions and (2) high-frequency random noise. During the FSS state in figure 9a, side load trajectories shift from low-frequency disturbances upstream –isolated over relatively narrow regions in space ($\pm\pi/2$)– to increasingly random high-frequency fluctuations downstream –distributed uniformly over the entire surface of the nozzle. Upon transitioning to the RSS state in figure 9b, the phase angle trajectories undergo a dramatic transformation. More coherent oscillations occur downstream at location x_3 and x_4 with phase angles covering a much broader region of space for a given period of time. Similar phenomena are observed at higher NPR conditions and so describe the dynamical characteristics that are unique to the RSS state. At NPR 50 in figure 9d, station x_1 is located at the foot of the incipient separation point where the separation shock resides (see figure 6d). At this location and NPR setting, the phase angle is relatively flat with occasional intermittent spikes. Periods of constant phase angle correspond to instances when the entire shock foot is located downstream of the transducer array at x_1. Likewise, the intermittent spikes reflect instances when the shock foot passes upstream and over a portion of the transducer array. These intermittent spikes are distributed randomly in space, once again, suggesting that the unsteady movement of the shock foot is axisymmetric in a statistically averaged sense.

(a), NPR 25, FSS

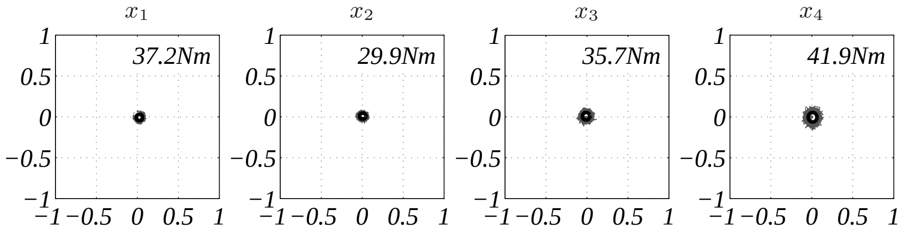

(b), NPR 30, RSS

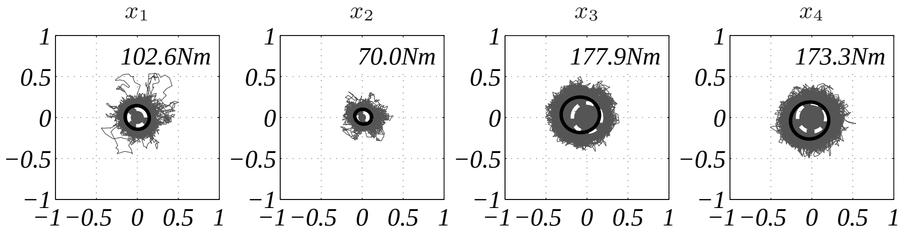

(c), NPR 40, RSS

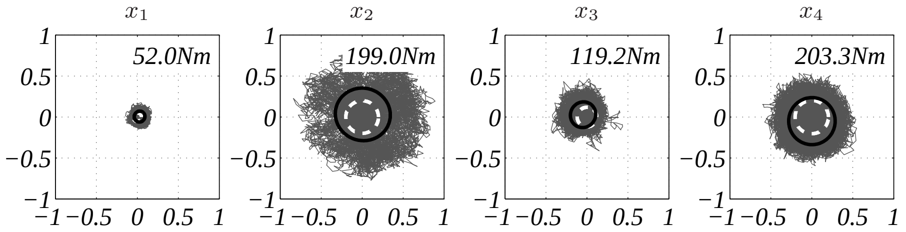

(d), NPR 50, RSS

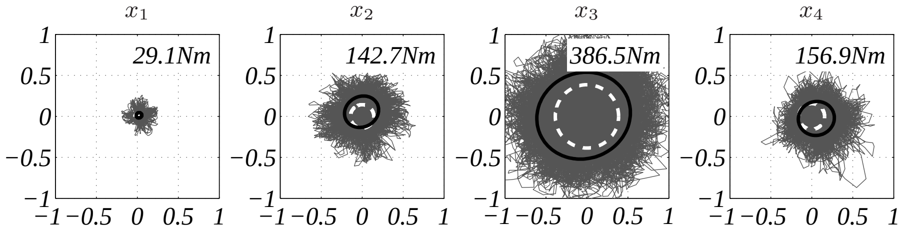

Fig. 8 Moment loci of the horizontal $M_H^{P,j}(t)$ and vertical $M_V^{P,j}(t)$ moments during a $2s$ period in [×1000 N-m]. Two additional lines identify the 95% confidence ellipse (solid dark −) and mean moment magnitude (dashed white −− and quantified in top right corner).

In the analysis so far, our attention has been restricted to spatially localized sources of side load activity based on a partitioning of the nozzle surface pressure into four individual stations. We will now consider the net resolved moment induced by the total dynamic surface pressure in an effort to reveal the net effects induced by coupled interactions (cancellation or amplification) of the perturbations at the four individual stations. This is obtained by superposing the moments induced

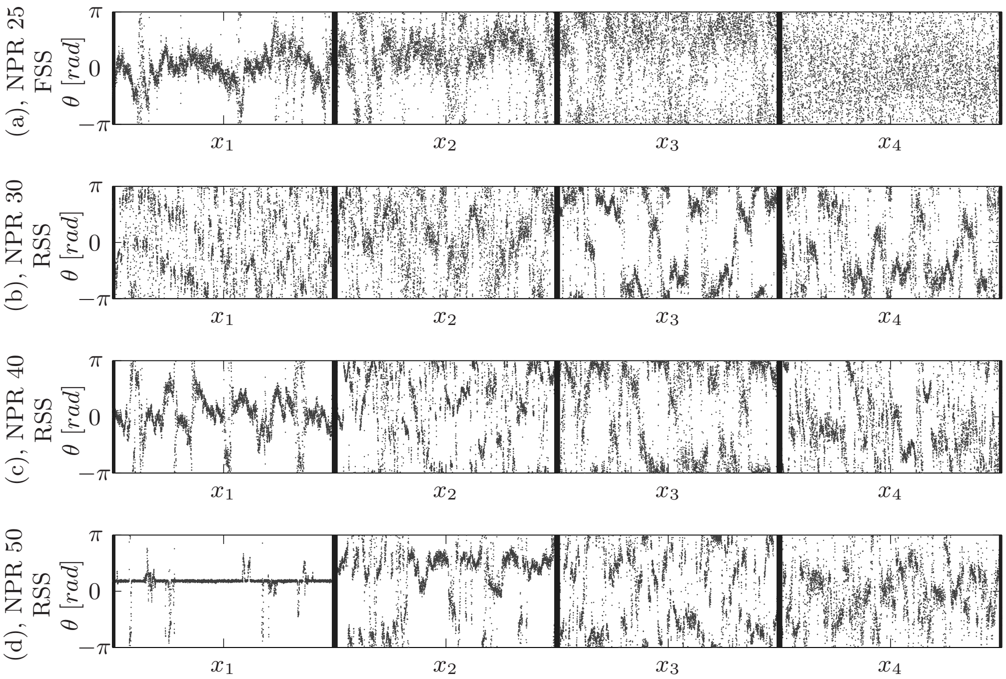

Fig. 9 Phase angle θ of the individual pressure based moment loci (figure 8) for a $0.25s$ period.

at all axial stations along the nozzle as follows,

$$M_H^P(t) = \sum_{j=1}^{4} M_H^j(t) \qquad \& \qquad M_V^P(t) = \sum_{j=1}^{4} M_V^j(t). \tag{6}$$

Here it is assumed that disturbances upstream of the first axial station are axisymmetric and so are neglected from the analysis. In the absence of any asymmetric unsteadiness or strong turbulent boundary layer fluctuations upstream of x_1, this assumption seems reasonable. The total resolved moment loci based on an integral of the entire unsteady surface pressure for each NPR is shown in figure 10a alongside the moment loci measured by the strain gauges in figure 10b. The findings between figures 10a and 10b are drastically different and so a discussion of plausible theories is soon provided. To begin, a summary of the time-averaged moment magnitudes identified in figure 8 have been itemized in table 1 along with the overhasty assumption of Eq. 5, an ensemble average of the time histories computed from Eq. 6 (denoted by ⟨Eq. 6⟩) and the mean moment magnitudes derived from the strain gauges (figure 10b).

Discrepancies in the results computed between Eq. 5 & ⟨Eq. 6⟩ and between ⟨Eq. 6⟩ & the strain

Table 1 Summary of time-averaged moment magnitudes at $x = x_M$ in [N-m].

	prediction based on pressure integration						response moment
NPR	x_1	x_2	x_3	x_4	Eq. 5	⟨Eq. 6⟩	(strain gauges)
25, FSS	37.2	29.9	35.7	41.9	144.7	89.8	169.1
30, RSS	102.6	70.0	177.9	173.3	523.8	352.8	59.8
40, RSS	52.0	199.0	119.2	203.3	573.5	244.2	74.3
50, RSS	29.1	142.7	386.5	156.9	715.2	316.2	146.8

gauges are linked to several plausible phenomena. The first is a consequence of dynamic coupling between different axial stations on the surface of the nozzle. These coupled interactions are related to a phase mismatch in either the azimuthal or temporal disposition of the side load pulsations produced by the first and second annular separation bubble (and associated shock motions). The smaller net resolved energy found in ⟨Eq. 6⟩ relative to Eq. 5 suggests that, on average, more events cancel than amplify. Synchronized measurements of the unsteady pressure with the velocity field in the vicinity of the interior surface of the nozzle would help explain this phenomena but are currently unavailable. As for the mismatch between the predicted pressure moments and strain tube measurements, two explanations are plausible. The first is attributed to the sparse spatial resolution of the pressure array and is believed to be mainly responsible for the discrepancies. If coupling between upstream and downstream stations is to occur, the current transducer arrangement may not have been fine enough to resolve events occurring between axial stations on the array. The second reason is attributed to the lack of consideration for dynamic and aeroelastic damping of the nozzle/strain tube assembly. The latter is less plausible since there is only one structural resonance in the frequency range of consideration and the bandwidth of this resonance contributes less than 5% to the total resolved energy of the system.

V. Spectral Analysis of Wall Pressure Mode Decomposition

It was concluded in the previous section that the majority of the observed side loads are caused by an unsteady pulsation and/or movement of the annular flow structures in the reattached jet along the nozzle wall. In many ways this circumferential unsteadiness is similar to SWTBLI observed by Ganapathisubramani *et al.* (2009) [28] in planar 2d compression ramp studies where the shock front position varies along the spanwise coordinate. In an effort to understand these spanwise modes in the (a), moment loci at $x = x_M$ due to asymmetric wall pressure distributions

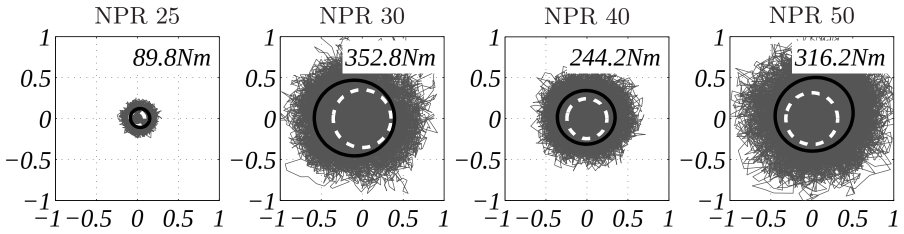

(b), moment loci at $x = x_M$ based on strain gauges

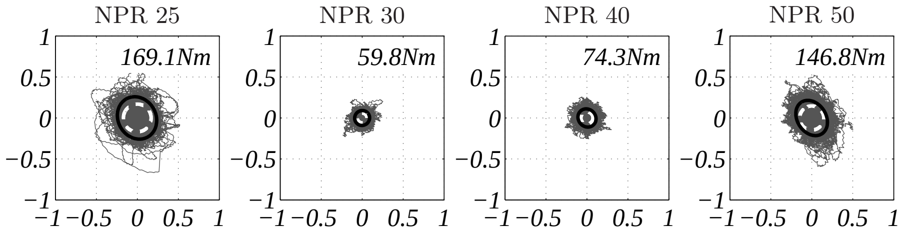

Fig. 10 Moment loci of (a) total pressure induced moment and (b) response moment measured by tube strain gauges during a $2s$ period in [$\times 1000$ N-m]. Two additional lines identify the 95% confidence ellipse (solid dark $-$) and mean moment magnitude (dashed white $--$ and quantified in top right corner).

conical geometry, a Fourier-azimuthal decomposition of the fluctuating surface pressure signatures is performed using the eight transducers located at each of the four axial stations.

A. Azimuthal Pressure Fourier Modes

The original high-frequency pressure field, $p\left(x, \theta, t\right)$, is Fourier transformed in azimuth to obtain the time-dependent complex Fourier coefficients,

$$p\left(x; m; t\right) = \mathcal{F}\left[p\left(x, \theta, t\right)\right]_{\theta}, \tag{7}$$

where m indicates the mode number. Five physical Fourier modes exist for the eight point azimuthal grid and the pressure decomposition is now presented as,

$$p\left(x, \theta, t\right) = \sum_{m=0}^{4} p^{m}\left(x, \theta, t\right), \tag{8}$$

where the m^{th} contribution to the original unsteady signal, $p^{m}\left(x, \theta, t\right)$, is obtained by inverse Fourier transforming Eq. (7) after selectively filtering discrete mode frequency combinations (positive and negative). As an illustration, the Fourier modes at a single position $x_j = \tilde{x}$ and one time step $t = \tilde{t}$ are presented in figure 11 according to the parameterization in polar coordinates as shown in Eq. (9). Only the first mode ($m = 1$ & $m = -1$) is responsible for side loads as indicated by the square which represents the peak of the resultant force.

$$R^m(\theta) \;=\; 1 + p^m\left(\tilde{x}, \theta, \tilde{t}\right), \qquad m = 0 \ldots 4, \qquad \theta \in [0, 2\pi). \tag{9}$$

(a), continuous azimuthal grid

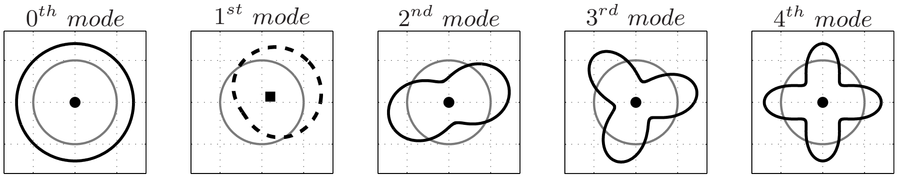

(b), course azimuthal grid (8 points)

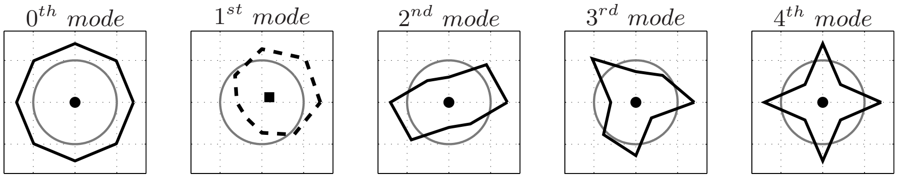

Fig. 11 An illustration of the azimuthal pressure Fourier modes (black) relative to the unit circle (grey).

For each NPR condition, the total resolved energy (TRE) per axial station is equal to

$$\Lambda(x) = \sum_m \lambda^{(m)}(x), \tag{10}$$

where $\lambda^{(m)}(x)$ is the variance of the m^{th} time-dependent Fourier-azimuthal mode coefficient $p(x; m; t)$. The magnitude of the TRE, for every NPR and axial station, is shown in figure 13a. The eigenspectra of the Fourier modes are presented as fractions of resolved energy per mode in figure 12 using the following normalization,

$$\alpha(x;m) = \frac{\lambda^{(m)}(x)}{\Lambda(x)}. \tag{11}$$

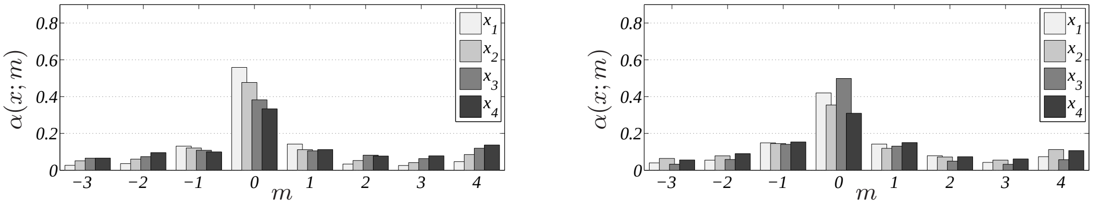

(a), NPR 25, FSS

(b), NPR 30, RSS

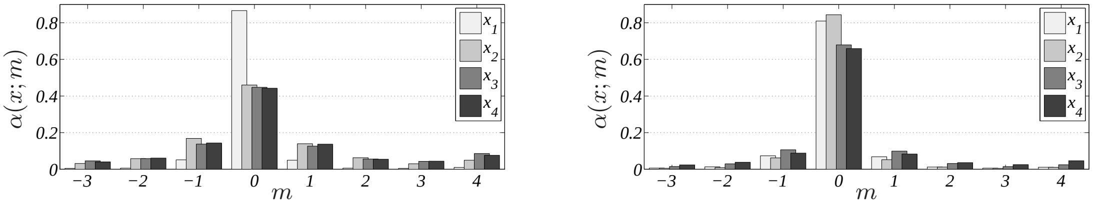

(c), NPR 40, RSS

(d), NPR 50, RSS

Fig. 12 Scaled eigenspectra of the azimuthal Fourier modes.

A non-trivial result is that for all cases investigated, the breathing mode ($m = 0$) dominates the energy wavenumber spectrum of the fluctuating surface pressure. During the FSS state, the energy of the breathing mode decreases with increasing axial distance, while the energy of mode one (the only mode responsible for side loads) remains relatively constant. Likewise, energy in the higher modes increases slightly. During the RSS state, energy in the breathing mode increases with increasing NPR. From the NPR 40 static pressure profiles in figure 6, it is observed that station x_1 is located closest to the incipient separation location and so the relatively dominant energy in the breathing mode suggests that the shock unsteadiness is relatively axisymmetric at this location.

B. Spectral Analysis of Pressure Fourier Modes

Power spectral densities of the time-dependent Fourier coefficients are computed to reveal the band of frequencies contained in each of the five Fourier-azimuthal modes. The PSD for each mode, given by Eq. (12), is presented in figure 13b for NPR 40 and location x_2.

$$G_{mm}(x; f) = \langle \hat{p}(x; m; f)\, \hat{p}^*(x; m; f) \rangle, \qquad \text{where } \hat{p}(x; m; f) = \mathcal{F}\left[p(x; m; t)\right]_t. \tag{12}$$

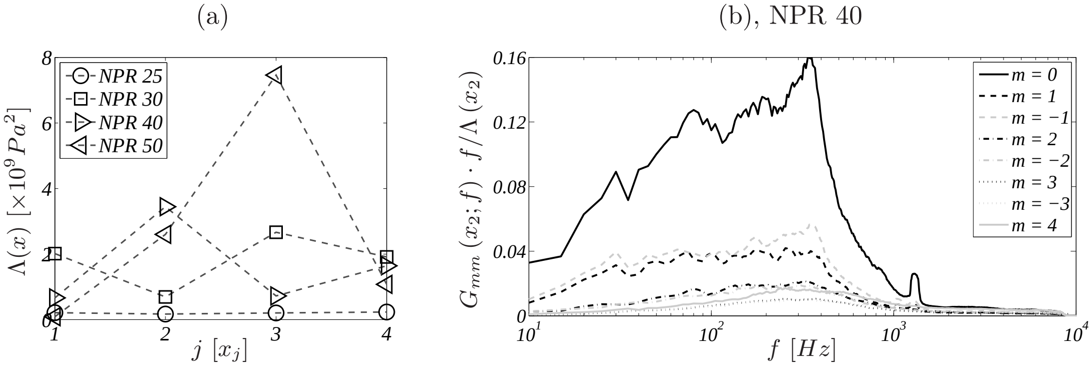

Fig. 13 (a) Total resolved energy for the azimuthal pressure Fourier decomposition, (b) Normalized frequency-dependent eigenspectra of the Fourier coefficients for NPR 40 and axial location x_2.

The frequency-dependent spectra of the breathing mode (0^{th} mode) and the side load inducing mode (1^{st} mode) are plotted for each NPR and axial location in figures 14 and 15, since most of the TRE is present in these modes. Compared to the spectra in figure 6, it can be observed how the original frequency-dependent energy content of the raw transducers is distributed over the first two Fourier modes. As an example, the raw PSD of the unsteady surface pressure at location x_3 and NPR 30 possesses relatively broadband features in the range $20Hz < f < 400Hz$ (figure 6f). In figures 14b and 15b, it can be seen how the high-frequency energy corresponds to the symmetric breathing mode, while low-frequencies are linked to the side load inducing mode. This is not the case for all axial stations and NPR conditions, as in other instances the low- and high-frequencies switch to axisymmetric and asymmetric type pressure signatures. The location of the transducer array relative to the locations of the shock foot play a crucial role in developing a complete understanding of this complicated phenomenon.

C. Correlation of the Wall Pressures and Response Moments

A useful indicator of the coupling between the input and output of a single or multiple degree of freedom system is the coherence. Where the current analysis is concerned, the transfer of energy

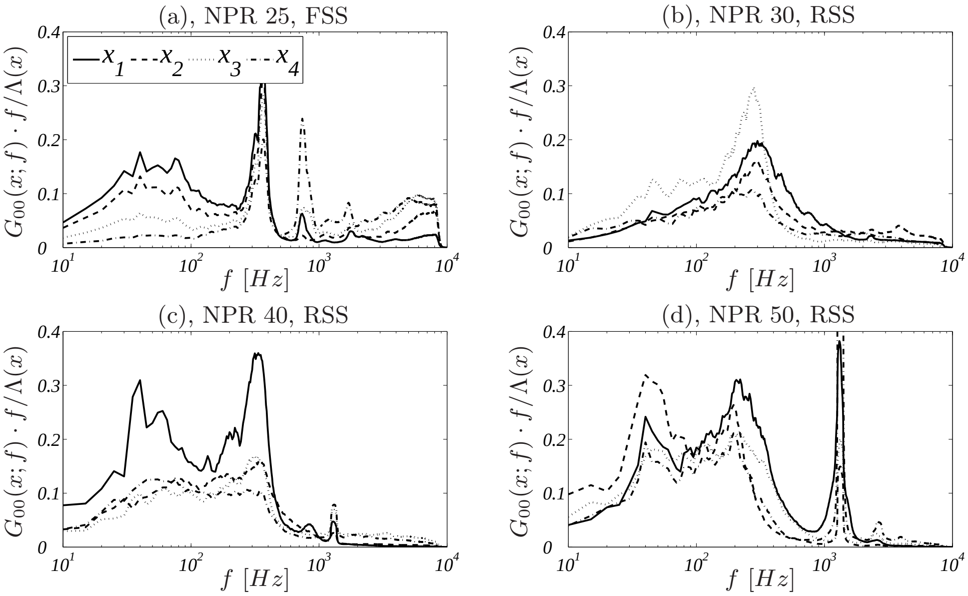

Fig. 14 Frequency-dependent eigenspectra of the 0^{th} Fourier mode (breathing mode).

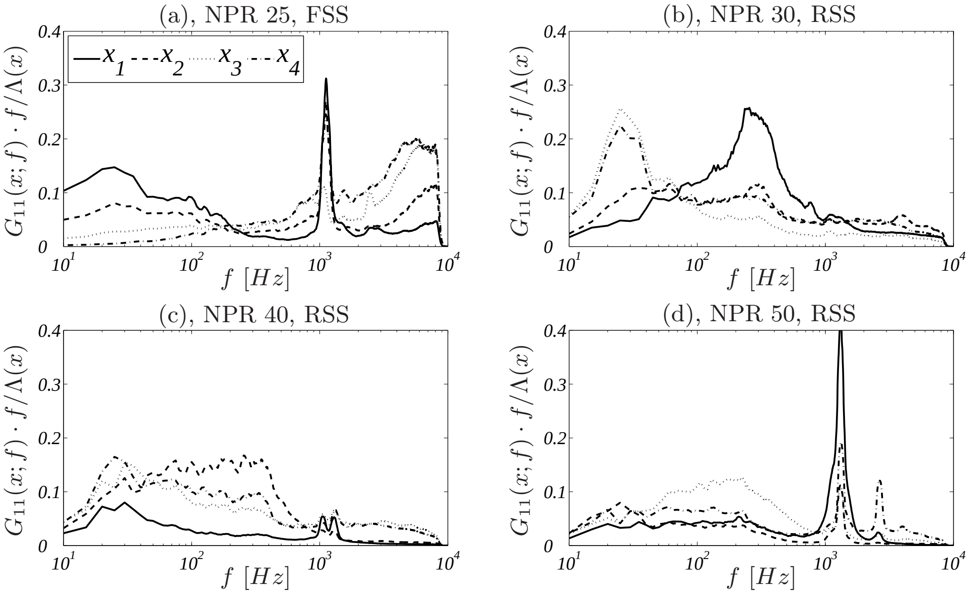

Fig. 15 Frequency-dependent eigenspectra of the 1^{st} Fourier mode (side load inducing mode).

between the wall pressures (excitation) and strain gauge moments (response) is quantified using the $m = 1$ pressure Fourier mode. It was previously shown how severe discrepancies between the net resolved moment loci (calculated from surface pressure alone) and the response from the strain gauges made it difficult to pinpoint the mechanisms responsible for producing the overall side loads (see figure 10). The coherence is here computed in an effort to shed some light on the sources of net disturbance and is computed using a linear transfer kernel between the first Fourier-azimuthal pressure mode and the strain data according to

$$\gamma_{ms}^{2}\left(x;f\right)=\frac{|G_{ms}(x;f)|^{2}}{G_{mm}(x;f)G_{ss}(f)}, \tag{13}$$

where $G_{ms}(x;f)$ is the cross spectral density between the m^{th} $(m=1 \ \vee \ m=-1)$ azimuthal pressure mode at location x and the moment time-series resulting from the strain gauge signals. $G_{ss}(f)$ is the PSD of the strain gauge response moment and is presented in figure 16 for each NPR (horizontal component only since the vertical component is very similar due to statistical invariance of the moment direction). The correlation can either be performed with the horizontal (mode $m=-1$ and strain moment signal $M_H^S(t)$) or vertical components (mode $m=1$ and $M_V^S(t)$). Only the coherence spectra of the first Fourier-azimuthal mode are shown since the coherence between the axisymmetric mode and the response moments produced very low levels, as would be expected.

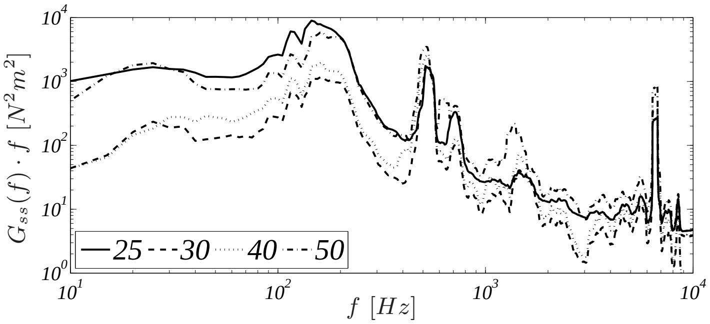

Fig. 16 PSDs of the horizontal response moments measured by the strain gauges, $M_H^S(t)$, at $x=x_M$.

In figure 17a, a strong linear coherence is clearly evident along the low-frequency part of the spectra during the FSS state and at axial locations corresponding to the separated flow in the vicinity of the separation. Similar findings are observed during RSS states, albeit the levels are not as strong. These smaller levels during RSS conditions lends more support to the idea of a phase mismatch in the space/time disposition of the side load pulsations.

For all instances measured, coherence levels fell rapidly at higher frequencies, owing to the fact that for single degree–of–freedom systems, the structural response becomes highly attenuated above

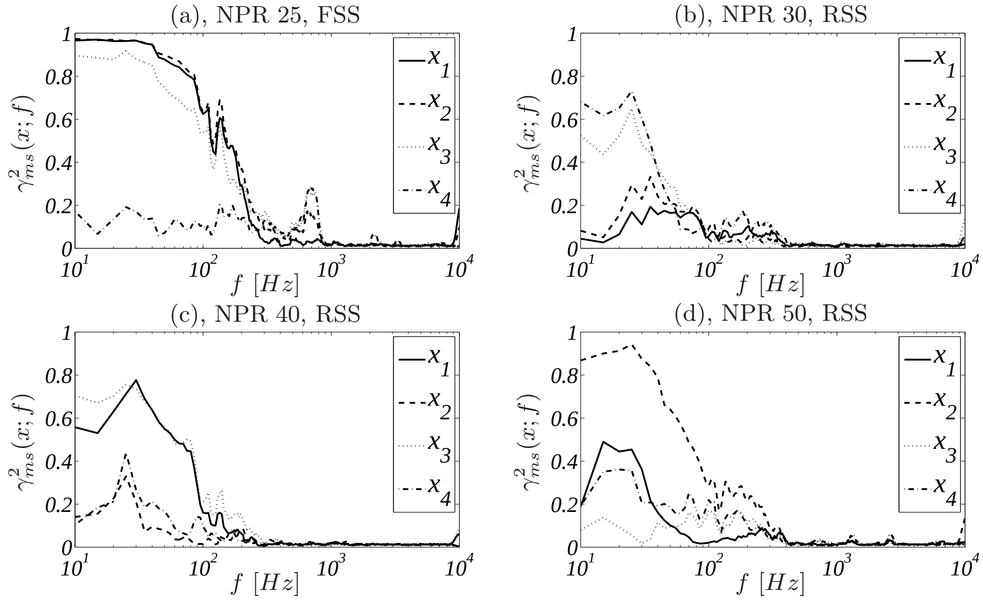

Fig. 17 Linear coherence spectra between pressure induced moment and strain gauge response (horizontal component).

1.4 times the natural frequency of the system. The natural frequency of this nozzle/strain tube assembly was measured to be $187Hz$ thus explaining the rapid roll-off in coherence in figure 17.

VI. Summary

The unsteadiness invoked by separation, and occasional reattachment, of the flow through highly overexpanded rocket nozzles was investigated experimentally on a sub-scale, cold-flow, TOP nozzle. Both dynamic wall pressure measurements and response moments of the nozzle/strain tube assembly were acquired at four constant nozzle pressure ratios (fluctuations superposed a steady mean flow) encompassing both FSS and RSS states. Spectral analysis of the dynamic surface pressure during FSS conditions revealed two distinct humps typical of SWTBLI phenomena. The first was found upstream near the foot of the separation shock and was dominated by low-frequency unsteadiness, while the second comprised more broadband high-frequency noise that grew in energy with increasing distance downstream. Upon transitioning to the RSS state, the separation between low and high-frequency humps became less distinct and was attributed to the increased complexity in the flow due to the formation of several incident and reflected shock wave patterns that are able to trap annular separation bubbles along the nozzle wall. A Fourier-azimuthal decomposition of the unsteady pressure revealed how the breathing mode encompassed most of the total resolved energy with the side load inducing mode comprising less than half.

An estimate of the response moments based on a localized integration of the unsteady wall pressures revealed how the most energetic side load inducing moments occur during the RSS state. Contrary to these findings, direct measurements of the response moments from the strain tube assembly revealed how the FSS state produces the greatest side load activity. The discrepancies between these two findings are attributed to a dynamic coupling between the annular separation bubbles located at different axial stations along the nozzle wall. The smaller net amplitudes measured by the strain gauges suggest that a spatial or temporal phase mismatch between successive annular separation bubbles produces more cancellations. Detailed surveys of the velocity field in the vicinity of the separated region are currently being conducted and will shed more insight in the nature of these interactions.

References

[1] Ruf, J. H., McDaniels, D. M., and Brown, A. M., "Nozzle Side Load Testing and Analysis at Marshall Space Flight Center," *45th AIAA/ASME/SAE/ASEE Joint Propulsion Conference and Exhibit*, AIAA, Denver, Colorado, Aug. 2009, AIAA Paper 2009-4856.

[2] Hagemann, G., Alting, J., and Preclik, D., "Scalability for Rocket Nozzle Flows Based on Subscale and Full-Scale Testing," *Journal of Propulsion and Power*, Vol. 19, No. 3, May 2003, pp. 321–331.

[3] Watanabe, Y., Sakazume, N., and Tsuboi, M., "LE-7A Engine Nozzle Problems during the Transient Operations," *38th AIAA/ASME/SAE/ASEE Joint Propulsion Conference and Exhibit*, AIAA, Indianapolis, Indiana, July 2002, AIAA Paper 2002-3841.

[4] Frey, M. and Hagemann, G., "Restricted Shock Separation in Rocket Nozzles," *Journal of Propulsion and Power*, Vol. 16, No. 3, May 2000, pp. 478–484.

[5] Arens, M. and Spiegler, E., "Shock-Induced Boundary Layer Separation in Overexpanded Conical Exhaust Nozzles," *AIAA Journal*, Vol. 1, No. 3, March 1963, pp. 578–581.

[6] Nave, L. H. and Coffey, G. H., "Sea Level Side Loads in High-Area-Ratio Rocket Engines," *AIAA/SAE 9th Propulsion Conference*, AIAA, Las Vegas, Nevada, Nov. 1973, AIAA Paper 1973-1284.

[7] Schmucker, R. H., "Flow Processes in Overexpanded Chemical Rocket Nozzles. Part 1: Flow Separation," original TUM-LRT-TB-7, translation NASA TM-77396, Technische Universität, Munich,

Lehrstuhl für Raumfahrttechnik, Munich, Germany, July 1973.

[8] Schmucker, R. H., "Flow Processes in Overexpanded Chemical Rocket Nozzles. Part 2: Side Loads Due To Asymmetric Separation," original TUM-LRT-TB-10, translation NASA TM-77395, Technische Universität, Munich, Lehrstuhl für Raumfahrttechnik, Munich, Germany, Sept. 1973.

[9] Hagemann, G., Frey, M., and Koschel, W., "Appearance of Restricted Shock Separation in Rocket Nozzles," *Journal of Propulsion and Power*, Vol. 18, No. 3, May 2002, pp. 577–584.

[10] Verma, S. B. and Haidn, O., "Study of Restricted Shock Separation Phenomena in a Thrust Optimized Parabolic Nozzle," *Journal of Propulsion and Power*, Vol. 25, No. 5, Sept. 2009, pp. 1046–1057.

[11] Ruf, J. H., McDaniels, D. M., and Brown, A. M., "Details of Side Load Test Data and Analysis for a Truncated Ideal Contour Nozzle and a Parabolic Contour Nozzle," *46th AIAA/ASME/SAE/ASEE Joint Propulsion Conference and Exhibit*, AIAA, Nashville, TN, July 2010, AIAA Paper 2010-6813.

[12] Östlund, J., Damgaard, T., and Frey, M., "Side-Load Phenomena in Highly Overexpanded Rocket Nozzles," *Journal of Propulsion and Power*, Vol. 20, No. 4, July 2004, pp. 695–704.

[13] Brown, A. M., Ruf, J., Reed, D., D'Agostino, M., and Keanini, R., "Characterization of Side Load Phenomena using Measurement of Fluid/Structure Interaction," *38th AIAA/ASME/SAE/ASEE Joint Propulsion Conference and Exhibit*, AIAA, Indianapolis, Indiana, July 2002, AIAA Paper 2002-3999.

[14] Chen, C. L. and Chakravarthy, S. R., "Numerical Investigation of Separated Nozzle Flows," *AIAA Journal*, Vol. 32, No. 9, Sept. 1994, pp. 1836–1843.

[15] Deck, S. and Guillen, P., "Numerical Simulation of Side Loads in an Ideal Truncated Nozzle," *Journal of Propulsion and Power*, Vol. 18, No. 2, March 2002, pp. 261–269.

[16] Schwane, R. and Xia, Y., "Time-Accurate CFD Predictions and Data Validation for Side Load Generation by Flow-Structure Coupling in Over-Expanded Rocket Nozzles," *Journal of Mathematical Modelling and Algorithms*, 2005.

[17] Wang, T. S., "Transient three-dimensional startup side load analysis of a regeneratively cooled nozzle," *Shock Waves*, Vol. 19, No. 3, July 2009, pp. 251–264.

[18] Verma, S. B., Stark, R., and Haidn, O., "Relation between shock unsteadiness and the origin of side-loads inside a thrust optimized parabolic rocket nozzle," *Aerospace Science and Technology*, Vol. 10, July 2006.

[19] Verma, S. B., "Shock unsteadiness in a thrust optimized parabolic nozzle," *Shock Waves*, Vol. 19, No. 3, July 2009, pp. 193–212.

[20] Erengil, M. E. and Dolling, D. S., "Unsteady Wave Structure near Separation in a Mach 5 Compression Ramp Interaction," *AIAA Journal*, Vol. 29, No. 5, May 1991, pp. 728–735.

[21] Humble, R. A., Scarano, F., and van Oudheusden, B. W., "Unsteady aspects of an incident shock wave/turbulent boundary layer interaction," *Journal of Fluid Mechanics*, 2009.

[22] Clemens, N. T. and Narayanaswamy, V., "Shock/Turbulent Boundary Layer Interactions: Review of Recent Work on Sources of Unsteadiness (Invited)," *27th AIAA Applied Aerodynamics Meeting and Exhibit*, AIAA, San Antonio, Texas, June 2009, AIAA-2009-3710.

[23] Nguyen, A. T., Deniau, H., Girard, S., and Alziary de Roquefort, T., "Wall Pressure Fluctuations in an Over-Expanded Rocket Nozzle," *38th AIAA/ASME/SAE/ASEE Joint Propulsion Conference and Exhibit*, AIAA, Indianapolis, Indiana, July 2002, AIAA Paper 2002-4001.

[24] Nguyen, A. T., Deniau, H., Girard, S., and Alziary de Roquefort, T., "Unsteadiness of Flow Separation and End-Effects Regime in a Thrust-Optimized Contour Rocket Nozzle," *Flow, Turbulence and Combustion*, 2003.

[25] Dumnov, G. E., "Unsteady side-loads acting on the nozzle with developed separation zone," *32nd AIAA/ASME/SAE/ASEE Joint Propulsion Conference and Exhibit*, AIAA, Lake Buena Vista, Florida, July 1996, AIAA Paper 1996-3220.

[26] Ruf, J. H., McDaniels, D. M., and Brown, A. M., "Cold Flow Test Results for Nozzle Side Loads for J-2X and SSME Test Articles," *57th JANNAF Propulsion Meeting*, JANNAF, Colorado Springs, Colorado, May 2010.

[27] Brown, A. M., Ruf, J. H., and McDaniels, D. M., "Recovering Aerodynamic Side Loads on Rocket Nozzles using Quasi-Static Strain-Gage Measurements," *50th AIAA/ASME/ASCE/AHS/ASC Structures, Structural Dynamics, and Materials Conference*, AIAA, Palm Springs, California, May 2009, AIAA Paper 2009-2681.

[28] Ganapathisubramani, B., Clemens, N. T., and Dolling, D. S., "Low-frequency dynamics of shock-induced separation in a compression ramp interaction," *Journal of Fluid Mechanics*, Vol. 636, 2009.

[29] Detailed flow measurements of the nozzle internal flow and shock pattern from this nozzle are currently unavailable.